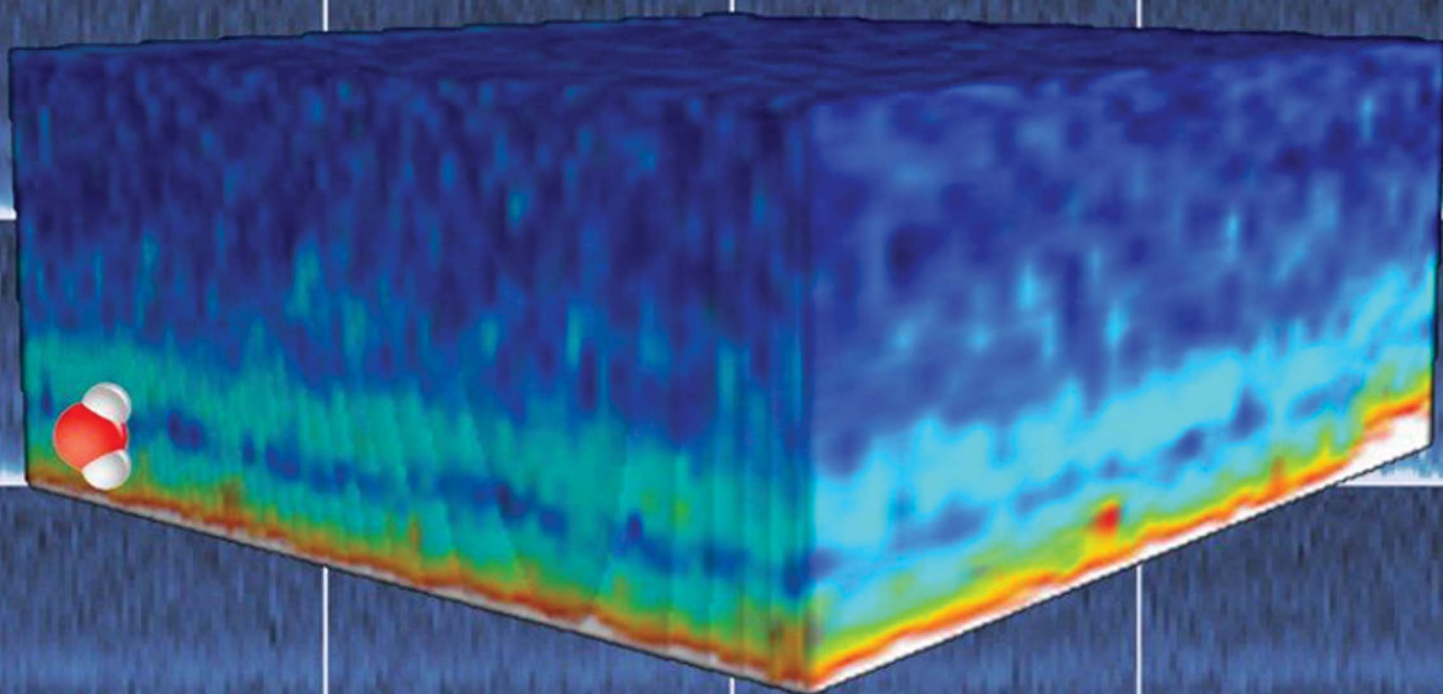


# Nanoscale

www.rsc.org/nanoscale

Volume 5 | Number 7 | 7 April 2013 | Pages 2535–3084



ISSN 2040-3364

RSC Publishing

**PAPER**

Ricardo Garcia *et al.*  
Three-dimensional quantitative force  
maps in liquid with 10 piconewton,  
angstrom and sub-minute resolutions



**NCNST**

# Three-dimensional quantitative force maps in liquid with 10 piconewton, angstrom and sub-minute resolution†

Cite this: *Nanoscale*, 2013, 5, 2678

Elena T. Herruzo,<sup>a</sup> Hitoshi Asakawa,<sup>b</sup> Takeshi Fukuma<sup>\*bc</sup> and Ricardo Garcia<sup>\*a</sup>

We develop a bimodal force microscopy method to map the three-dimensional force fields and their time-evolution on a variety of solid–water interfaces. The force maps show an oscillatory decaying force perpendicular to the solid surface with a 0.3 nm periodicity. The technique enables the three-dimensional imaging and mapping of the hydration layers and forces on mica and protein GroEL surfaces with 10 piconewton, 2 angstrom and 40 second (whole volume) resolutions. We record the existence and evolution of nanoscale perturbations involving thousands of water molecules of the protein–liquid interface. Those instabilities are not found in stiff and atomically flat interfaces.

Received 5th October 2012

Accepted 18th November 2012

DOI: 10.1039/c2nr33051b

[www.rsc.org/nanoscale](http://www.rsc.org/nanoscale)

## 1 Introduction

Forces in the sub-nanonewton range are applied to generate atomic and molecular resolution images of surfaces.<sup>1–5</sup> Forces in the 1–100 piconewton range are the fingerprints of single molecule interactions.<sup>6–9</sup> A large variety of biomolecular processes involve time scales in the 1 ms to 1 s range.<sup>2,6,8–10</sup> Many applications in materials science and cell biology would benefit from the three-dimensional mapping of interactions with angstrom, millisecond and piconewton resolutions.

The adsorbed water molecules have a key role in many interfacial biological processes such as ion diffusion.<sup>9</sup> Water molecules and layers are spontaneously adsorbed onto surfaces under ambient conditions.<sup>11,12</sup> This process modifies several interfacial properties such as adhesion, friction or lubrication.<sup>13,14</sup> Therefore to understand with molecular detail many interfacial phenomena it requires the development of novel nanoscale microscopy methods. Here, we develop a force microscopy method to map the three-dimensional force fields and their time-evolution on a variety of solid–water interfaces. We map forces on soft and stiff–water interfaces with 10 piconewton, 2 angstrom and 5 millisecond resolutions. Above the solid surface, the maps show an oscillatory decaying force perpendicular to the solid surface with a 0.3 nm periodicity. The force maps on a model stiff sample such as mica are stable over the observation period. However, on a soft sample such as

arrays of chaperonins, the oscillatory pattern is punctuated by the presence of sudden force changes of about 200 pN. Those fluctuations involve the motion of several thousands of water molecules. Our three-dimensional maps could enable a complete characterization of solid–liquid interfaces and, in particular, to follow biomolecular processes on cell surfaces with molecular resolution.

The polar character of the water molecules and some of the amino acid residues in the polypeptide chains of the proteins promotes the adsorption of water molecules on biomolecular surfaces. The hydration of a protein influences its stability and function. Thus, the adsorbed water molecules have a key role in interfacial biological processes.<sup>9,10</sup> The above considerations have been a driving factor in the evolution of atomic force microscopy (AFM) from operating in a vacuum<sup>1</sup> to image in real time protein–protein interactions in liquid.<sup>2</sup> Furthermore, water molecules and layers are spontaneously adsorbed onto surfaces under ambient conditions.<sup>11–14</sup> This process modifies several interfacial properties such as adhesion, friction or lubrication.<sup>13,14</sup> Water layers forming nanoscale liquid bridges are used to develop nanolithographies.<sup>15</sup> Therefore to understand with molecular detail many interfacial phenomena in aqueous environments, in particular those involving biomolecules and cell surfaces it requires the development of microscopy methods that provide images and force maps as a function of the position in three dimensions with high spatial, time and force resolutions.

Holscher *et al.*<sup>16</sup> and Schwarz and co-workers<sup>17,18</sup> demonstrated the ability of a frequency modulated AFM operated in ultra-high vacuum to image the force and energy profiles with atomic resolution in *x*, *y* and *z*. Those experiments were performed by taking sequentially *xy* data at different heights. Then, the collected data were combined to form a dense (*x*, *y*, *z*,  $\Delta f$ )

<sup>a</sup>Instituto de Ciencia de Materiales de Madrid (CSIC), 28049 Madrid, Spain. E-mail: r.garcia@csic.es

<sup>b</sup>Bio-AFM Frontier Research Center, Kanazawa University, Kakuma-machi, Kanazawa 920-1192, Japan

<sup>c</sup>Division of Electronic and Computer Engineering, Kanazawa University, Kakuma-machi, Kanazawa 920-1192, Japan. E-mail: fukuma@staff.kanazawa-u.ac.jp

† Electronic supplementary information (ESI) available. See DOI: 10.1039/c2nr33051b

array, where  $\Delta f$  is the change in frequency. Fukuma *et al.*<sup>19</sup> and Kimura *et al.*<sup>20</sup> extended three-dimensional AFM into liquid environments. At the same time, their approaches significantly reduced the acquisition time. In the latter, the images were generated by taking multiple force *versus* distance curves in an *xy* plane.<sup>20</sup> This approach reduced the acquisition time from hours to several minutes. A further reduction in the acquisition time was achieved by modulating the *z* position of the tip while the probe is scanned laterally with a distance feedback control.<sup>19</sup> Independently, multifrequency force microscopy,<sup>21</sup> in particular bimodal AFM,<sup>22</sup> has been developed to enhance the sensitivity to detect small forces and to map simultaneously different properties.<sup>23,24</sup>

In bimodal AFM<sup>23</sup> the microcantilever is simultaneously excited with two frequencies that are tuned at the first two eigenmodes. This generates four different observables the amplitudes and the phase shifts of the excited modes ( $A_i, \phi_i$ ). Those observables have different surface sensitivities.

Here we develop a force microscopy method that combines bimodal AFM operation and the generation of three-dimensional (3D) profiles to study the organization and time evolution of solid–liquid interfaces on stiff (mica) and soft-matter (proteins) surfaces. This instrument measures the static and dynamic three-dimensional force field of solid–water interfaces by detecting the changes in the AFM observables with the *xyz* position of the probe. Those changes are associated with variations in the forces acting between the tip and the water interface which, in turn, are related to changes of the solid–liquid interface such as the local stiffness or the density of the

water. The ability to detect very small amplitude changes (1 pm) enables us to obtain 3D atomic resolution images of the mica–water interface. On protein patches, we map the time evolution of the layering of the water molecules in the *z* direction while nanoscale resolution is achieved in the *xy* plane. The bimodal 3D-AFM enables us to increase the observed volume by a factor of 10.

## 2 Experimental section

### AFM microscopy

In bimodal 3D-AFM the tip scans the *xy* plane parallel to the sample surface as it is also displaced in the perpendicular *z* axis (Fig. 1a). The feedback mechanism acts on the amplitude  $A_1$ . It establishes a mean tip–surface distance  $z_c$  for imaging like in regular amplitude modulation AFM. Then the tip–surface separation is modulated as the tip scans laterally as  $z_c \pm \Delta z_m$  to generate the 3D maps of the solid–liquid interface. During the modulation, the observables will change following the changes of the interface. The bimodal 3D-AFM images were obtained with a home-made AFM head with a commercial controller (ARC, Asylum Research Inc., Santa Barbara, CA) modified to increase the detector signal-to-noise ratio. Bimodal AFM data acquisition was performed by using the UHFLI 600 MHz Lock-in Amplifier of Zurich Instruments.

The experiments were carried out by using a very sensitive and low noise cantilever deflection sensor<sup>25–27</sup> which enables the detection of very small amplitudes ( $\sim 1$  pm). Typical parameters

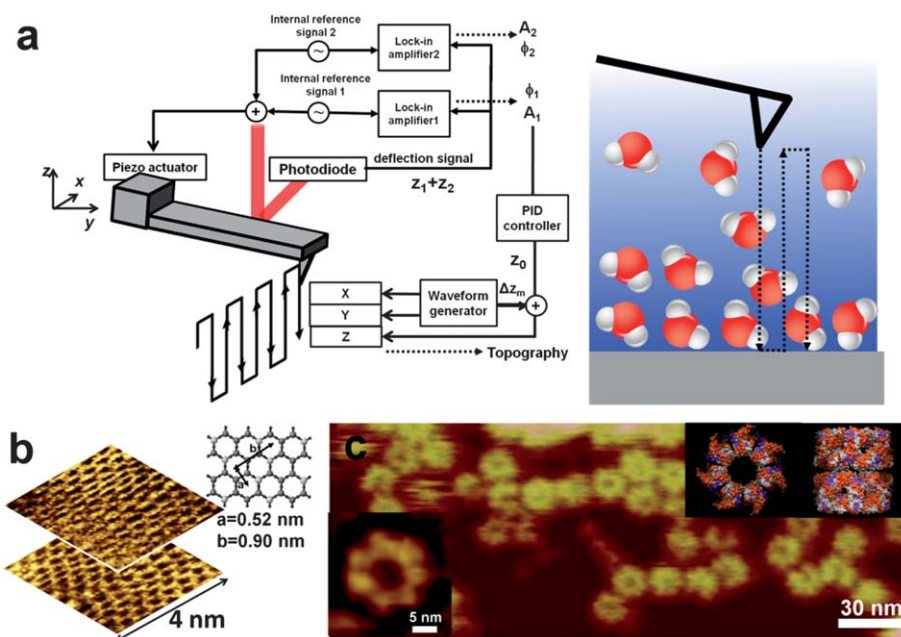


**Fig. 1** Diagram of bimodal 3D-AFM. (a) Block diagram of bimodal excitation and 3D modulation. In bimodal 3D-AFM the microcantilever is driven simultaneously at the frequencies of the first two flexural modes. Additionally a modulation is applied to the *z*-piezo ( $\Delta z_m$ ) at the same time that the tip is displaced over an *xy* plane of the interface (rectangular waveform). A scheme of the operation of the AFM in a solid–water interface is also shown. (b) Two different *xy* planes of a mica–water interface. The atomic periodicity of the mica is shown in the lower image. The images have been obtained from the bimodal 3D-AFM data. (c) Image of a patch of GroEL molecules in liquid. The lower inset shows a molecular resolution image (processed) of a single GroEL showing the seven subunits of the ring. The inset (upper right) shows the top view and side views of the GroEL structure as obtained by diffraction methods<sup>28</sup> (protein data bank 1KPO).

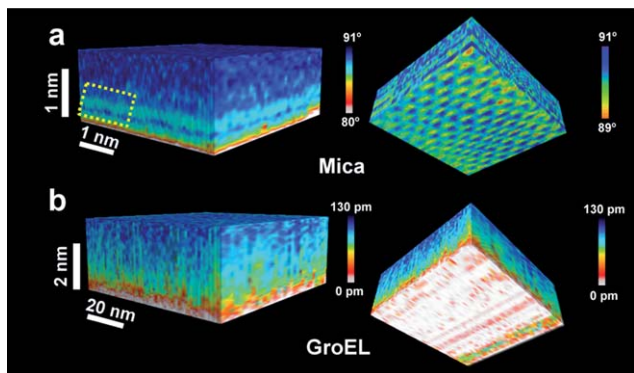


**Fig. 2** 3D images of solid–water volumes. (a) 3D map of a mica–water interface. The side view shows variations of  $\phi_2$ . The stripes are associated with the presence of hydration layers.  $A_{01} = 200$  pm,  $A_{02} = 6$  pm and  $A_{sp} = 100$  pm. The view from the mica surface upwards (right panel) shows variations of  $\phi_2$ . This image illustrates the compatibility between 3D imaging and angstrom resolution in the  $xyz$  plane. Oscillations in  $\phi_2$  due to the presence of hydration layers are highlighted in the yellow square. (b) 3D map of a GroEL patch–water interface. The side view shows a slightly rough landscape with variations of  $A_1$  of about 1 nm. Those variations are interpreted as perturbations in the interface. The view from the GroEL patch upwards shows the relative rough surface of the GroEL patches (see Fig. 1c).  $A_{01} = 500$  pm,  $A_{sp} = 250$  pm.

to generate the 3D-AFM images were free first mode amplitudes of  $A_{01} = 70$ – $200$  pm, set point amplitudes of  $A_{sp} = 35$ – $100$  pm and free second mode amplitudes of  $A_{02} = 3$ – $6$  pm. This instrument provides four different observables to record events at the solid–water interface ( $A_i, \phi_i$ ). The optimization of bimodal

AFM parameters for high resolution imaging is still an open problem. Here we have used several  $A_1/A_2$  ratios to capture the 3D-AFM images with the only criterion of using the combination that gave the highest resolution and contrast. The frequency of the  $\Delta z$  modulation was 195 Hz for the data recorded with 256 pixels and 98 Hz for the data with 512 pixels. The lateral speed was either  $6.1$  nm  $s^{-1}$  (Fig. 2) or  $12.2$  nm  $s^{-1}$  (Fig. S2†) for the images recording events in volumes of  $4 \times 4 \times 1.5$  nm<sup>3</sup>. The lateral speed was  $182$  nm  $s^{-1}$  for the 3D images in volumes of  $64 \times 64 \times 3$  nm<sup>3</sup>. The data were recorded with either 512 or 256 pixels in  $z$  and  $64 \times 64$  pixels in  $xy$ . Each  $xz$  frame was captured in either 0.66 s (256 pixels) or 1.3 s (512 pixels). The minimum time required to capture a bimodal 3D-AFM image was 42 s. The measurements were performed at room temperature ( $\sim 300$  K).

The bimodal 3D-AFM maps generate  $A_i = A_i(x,y,z)$  and  $\phi_i = \phi_i(x,y,z)$  data. By combining the amplitude and phase shift curves, it will be possible to reconstruct the force as a function of the distance (ESI†).

### Microcantilevers

Several cantilevers have been used to perform these experiments. Most of the data were obtained by using silicon cantilevers with force constant  $k_1 = 40$  N  $m^{-1}$ , resonant frequency  $f_{01} = 135$  kHz and quality factor  $Q_1 = 7$  (PPP-NCH: nanosensors). Fig. 1c was obtained with a silicon nitride cantilever of  $k_1 = 0.37$  N  $m^{-1}$ ,  $A_0 = 4$  nm and  $f_{01} = 13$  kHz (Olympus-OMCL-RC800PSA).

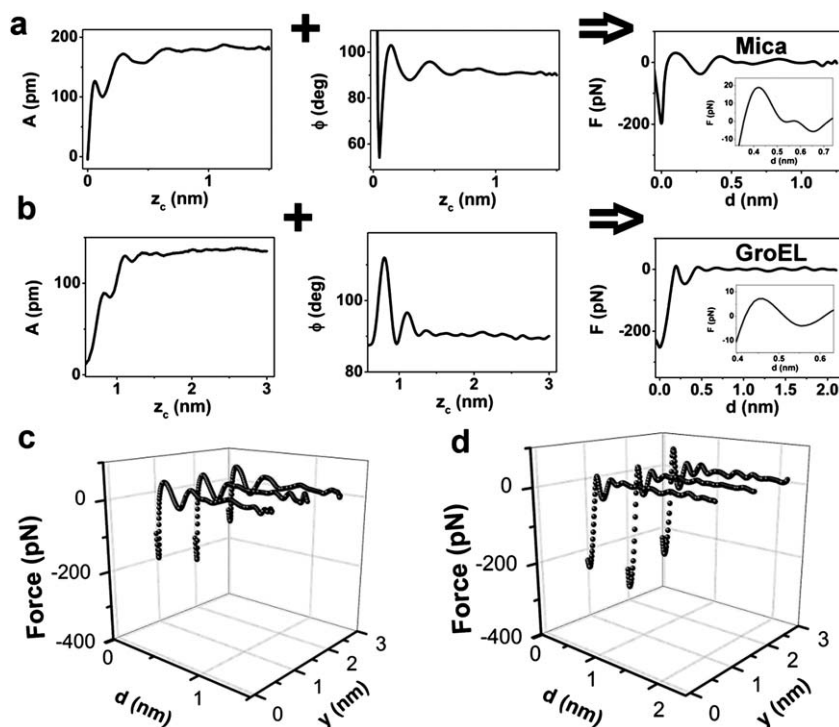


**Fig. 3** Force reconstruction from amplitude and phase shift data. (a) Amplitude and phase shift curves taken on a mica–water interface and the force curve deduced from them. The inset shows a section of the force curve with a resolution of 5 pN. (b) Amplitude and phase shift curves taken on a GroEL–water interface and the force curve deduced from them. (c) Force curves along different positions of the mica–water interface. (d) Force curves along different positions of the GroEL–water interface.

## Mica

Freshly cleaved muscovite mica was used as a solid substrate  $[\text{KAl}_2(\text{Si}_3\text{Al})\text{O}_{10}(\text{OH})_2]$ .

## Biological preparation

Two different protocols were followed to generate the GroEL patches on freshly cleaved muscovite mica. Most of the data were obtained by using GroEL (Chaperonin 60 – Sigma-Aldrich) which was dissolved until a protein concentration of  $50 \mu\text{g ml}^{-1}$  was obtained at pH 7.5. The buffer was prepared with 50 mM HEPES–KOH, 100 mM KCl, 5 mM  $\text{MgCl}_2$  and 1 mM DTT. After incubation on mica for 40 minutes, the sample was rinsed with a buffer prepared with 25 mM HEPES–KOH, 100 mM KCl and 5 mM  $\text{MgCl}_2$ . A drop of  $60 \mu\text{l}$  of the latter buffer was introduced in the AFM fluid cell for AFM imaging. Fig. 3a was obtained by using GroEL (Chaperonin 60 – Sigma-Aldrich) which was dissolved until a protein concentration of  $50 \mu\text{g ml}^{-1}$  was obtained at a pH 7.5. The buffer was prepared with 50 mM Tris–HCl, 150 mM KCl and 10 mM  $\text{MgCl}_2$ . After incubation on a freshly cleaved mica for 40 minutes, glutaraldehyde (25%) was added for 5 minutes, and the sample was rinsed with a buffer prepared with 25 mM Tris–HCl, 150 mM KCl and 10 mM  $\text{MgCl}_2$ . Finally the sample with GroEL deposited on mica was introduced in the AFM fluid cell which was filled with the latter buffer.

## 3 Results and discussion

Mica and GroEL have rather different surface structures (Fig. 1b and c) and mechanical properties. The elastic modulus for mica (basal plane) is about 50 GPa while for a single GroEL molecule we have measured a modulus of about 50 MPa. For imaging we conveniently choose the observable (amplitude or phase shift) that in the given experiment has the higher signal-to-noise ratio.

Fig. 2 shows the full three-dimensional data obtained on mica and on GroEL–water interfaces. There are two complementary ways to assemble the 3D maps by either presenting the data from the  $xz$  or the  $xy$  planes. On the mica, the bimodal 3D-AFM maps generally cover a small volume ( $4 \times 4 \times 1.5 \text{ nm}^3$ ) to show atomic resolution in the  $xy$  plane. Fig. 2a shows a 3D-AFM image of the mica–water interface formed by gathering  $xz$  data. In the proximity of the mica, the observables show some distinct oscillations (left panel). The observed periodicity is close to the nominal size of a water molecule which suggests the

presence of hydration layers. The 3D-AFM image formed by gathering  $xy$  planes as seen from the mica surface shows the atomic structure of the mica (Fig. 2a, right panel).

On the GroEL array, the bimodal 3D-AFM images cover regions of about  $64 \times 64 \times 3 \text{ nm}^3$  to include several proteins (Fig. 2b). The 3D-AFM maps taken on an array of GroEL molecules show a complex interface where the amplitude and the phase shift are punctuated by sudden changes. In this representation those fluctuations conceal the presence of oscillations in the vicinity of the GroEL patches. However, the oscillations would be revealed by presenting individual  $xz$  images (see Fig. 5b).

Ideally, during the modulation of the tip–surface separation, the AFM observables will change by following either the changes of the interaction force with the distance (static) or because a new object and/or interaction has been incorporated into the tip's field of view (dynamic). In vacuum or air, the forces should have a long-range tail coming from van der Waals and/or electrostatic interactions and a short-range repulsive force. In liquid, the long-range tail also contains contributions from the electrostatic double layer force. In addition, the discrete character of atoms and molecules in the liquid would originate the presence of oscillatory solvation forces.<sup>11–13</sup> Those forces are very small and require very high sensitive instruments to be detected or measured.<sup>26–34</sup> In the presence of hydration layers, we expect that the strength of the force sensed by the tip will change following the variations of the density or even velocity of the water in the solid–liquid interface. In this context, molecular dynamics simulations involving water molecules, a carbon nanotube tip and a flat OH-terminated alumina surfaces showed force oscillations associated with the presence of two interfacial water layers.<sup>35</sup> Those simulations reported oscillations in the repulsive force and in the density of the interfacial hydration layers as a function of the tip–surface separation.

Paradoxically, forces cannot be directly measured by dynamic force microscopy experiments. To recover the force from the dynamic AFM observables it requires the use of force inversion methods.<sup>36–41</sup> The accuracy and reliability of those methods have been contrasted by numerical simulations. We apply Katan *et al.* approach<sup>40</sup> to transform amplitude and phase shift curves into force  $F(x,y,z)$  maps (Fig. 3, see also ESI<sup>†</sup>). It is important to observe that the amplitude and the phase shift curves carry out complementary information about the surface properties.<sup>42</sup> In general the signal-to-noise ratio of the phase shift curves is slightly better than that of the corresponding amplitude curves (see Fig. 3a and b).

Fig. 3a displays the force curves as a function of the distance to the mica surface for three different positions along the  $y$  axis. The force curve has an absolute minimum when the tip touches the mica surface ( $-190 \text{ pN}$ ). In addition there are two local minima with negative forces (attractive) and two local maxima with positive values (repulsive). For separations 1 nm above the surface, the curve shows some fluctuations that reflect the background noise. The difference between contiguous local maximum and local minimum is, respectively, 25 pN and 70 pN. From the fluctuations far from the surface we estimate a force resolution of 10 pN. The minima, starting from the mica

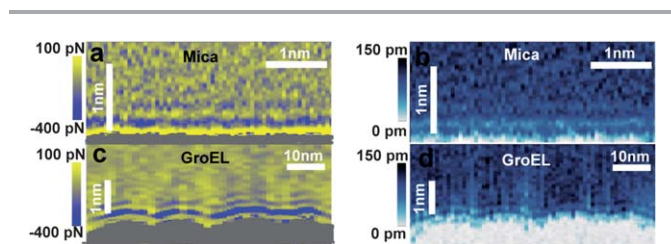


**Fig. 4** Section of a 3D force map. (a) Force map in an  $xz$  plane of a mica–water interface. (b) Amplitude image of the  $xz$  plane shown in (a). (c) Force map in an  $xz$  plane of a GroEL–water interface. (d) Amplitude image of the  $xz$  plane shown in (c).

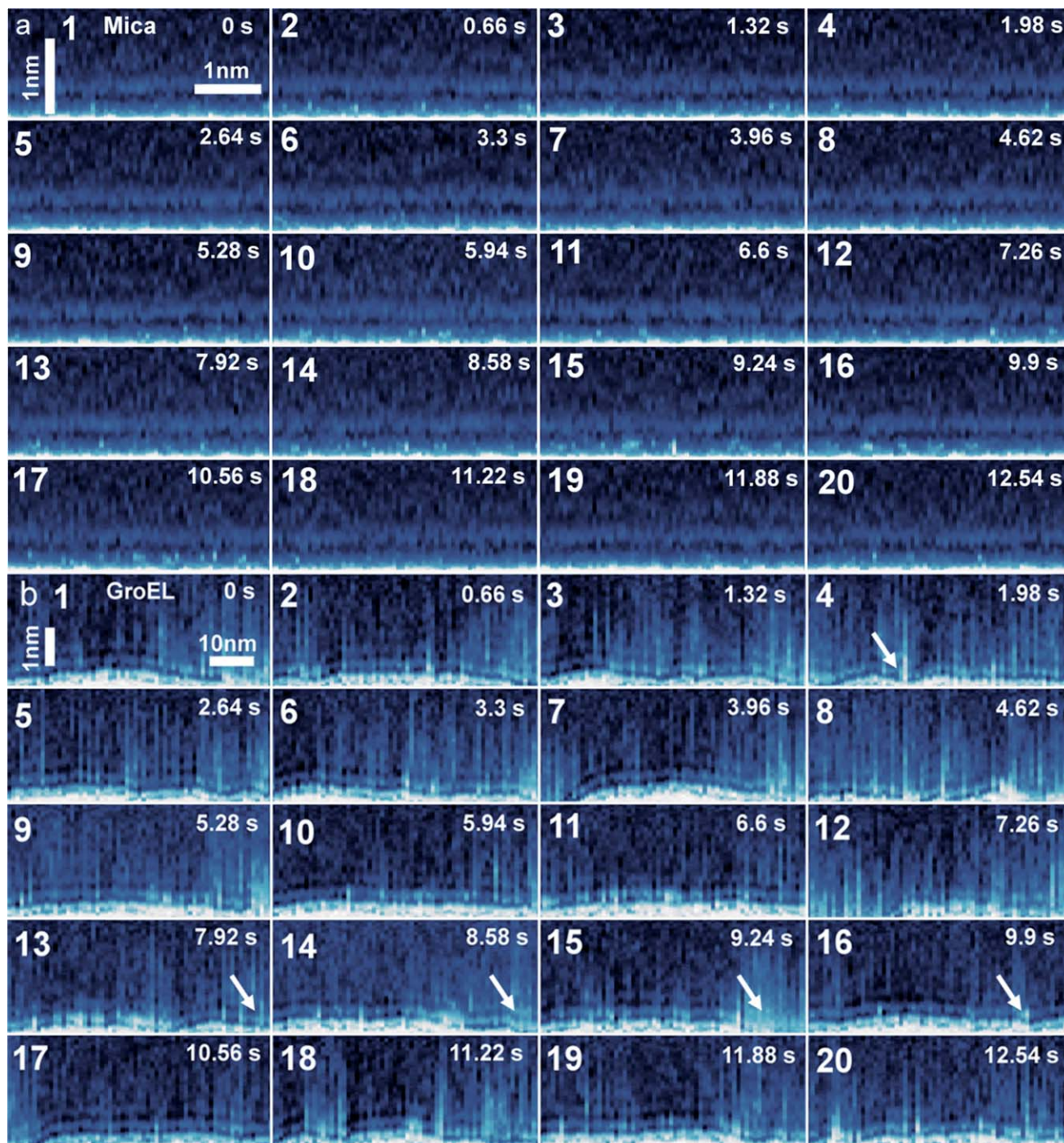


**Fig. 5** Bimodal 3D-AFM images of water monolayers in a solid–water interface. The presence of the hydration layers is revealed by the alternation of light and dark stripes above the solid surface. (a) Sequence of  $xz$  frames taken at different  $y$  positions in the mica–liquid interface. The frames are separated by 0.94 nm and 0.66 s, respectively, in the  $y$  and time axes. The hydration layers are very stable through the whole observation period. The white region at the bottom of the frames indicates the position of the mica. (b) Sequence of  $xz$  frames at different  $y$  positions in the GroEL–liquid interface. The frames are separated by 0.94 nm and 0.66 s, respectively, in  $y$  and time axes. Arrows indicate the position of some of the instabilities that disrupt the continuity of the hydration layers. In (a) the bimodal 3D-AFM maps show the variation of  $A_1(x,y,z)$  with  $A_{01} = 200$  pm,  $A_{02} = 6$  pm and  $A_{sp} = 100$  pm. In (b)  $A_{01} = 500$  pm,  $A_{sp} = 250$  pm.

surface, are separated, respectively by 0.27 nm and 0.37 nm. Those values match the values obtained from MD simulations. The 3D data enable to obtain the force curves as a function of the  $xy$  position (Fig. 3c). On mica, the curves have similar shapes but there are some differences in the attractive force

value at the tip–mica contact, probably due to a change of the contact area.

The same procedure is applied for the data recorded on GroEL patches. Fig. 3b shows the amplitude and phase shift curves and the corresponding force curve. To improve the

signal-to-noise ratio, the amplitude and phase shift curves are the average value of 30 individual curves. Two local minima with negative forces (attractive) and two maxima with positive values (repulsive) are observed. The difference between maximum and minimum is, respectively, 10 pN and 60 pN. The absolute minimum marks the start of the repulsive force upon mechanical contact with the GroEL surface ( $-245$  pN). The minima, starting from the mica surface, are separated, respectively by 0.3 nm and 0.25 nm. The 3D data enable to obtain the force curves as a function of the lateral position (Fig. 3d). We have avoided the regions of the GroEL–water interface with the presence of perturbations. In the stable regions the force curves show a periodicity associated with the presence of hydration layers and/or nanoconfined water.

The above procedure can be extended to generate force maps of  $xz$  planes. Fig. 4a shows the force map  $F(x,z)$  for a mica–water interface at a fixed  $y_0$ . The features observed in the force maps show a good correlation with the features observed in the amplitude image (Fig. 4b). Fig. 4c shows a force map obtained in a GroEL–water interface. The force map shows the contours of four GroEL molecules. The map also shows an oscillation of the force that is associated with oscillations in the density of the water in the vicinity of the protein surface. The corresponding amplitude image is shown in Fig. 4d.

Now we focus on using 3D maps and images to record some dynamic processes. The time evolution of the mica and GroEL–water interfaces is shown in Fig. 5. On mica, the map shows a region of a  $4 \times 1.9 \times 1.5$  nm<sup>3</sup> volume (Fig. 5a). The amplitude panels show the oscillation of the force as a function of the vertical position. The frames are consecutive (0.66 s apart). The

alternation of sections of higher and lower amplitudes indicates an oscillatory behavior in the interfacial forces. Those layers remain without vertical and lateral variations. This is corroborated by acquiring 3D-AFM images over larger volumes ( $60 \times 60 \times 3$  nm<sup>3</sup>) (data not shown).

The 3D-AFM map of the GroEL–water interface is shown in Fig. 5b. The frames cover a  $60 \times 20 \times 3$  nm<sup>3</sup> region. The frames are acquired consecutively (0.66 s apart). They are separated by about 1 nm in the  $y$  axis. The sequence of panels also records the presence and evolution of instabilities that disrupt the continuity of the hydration layers. Some of them involve a single pixel in the  $x$  axis (0.94 nm) and a few pixels in the  $z$  axis. Those instabilities are very localized because the hydration layer in neighboring  $x$  positions (1–2 nm apart) is unaffected. This type of perturbation cannot be followed because it has a time relaxation shorter than our time resolution. However, there are perturbations that involve the collective displacement of several thousands of water molecules which have a relaxation time larger than the instrumental resolution. The sequence captured in the right corner of frames 13–16 is an example. We have measured the force changes associated with those perturbations. For example, the average force in the lower right corner of frame 15 is increased about 200 pN with respect to the same region in frame 14. In many cases, the perturbations seem to be originated in the rougher regions of the protein surface, for example, in the gaps between proteins (see Fig. 1b). Frame 4 (Fig. 5b) shows a perturbation that appears to be pinned down in the region that separates two proteins. In some cases we have observed fluctuations in regions where the protein surface does not show any significant height changes.

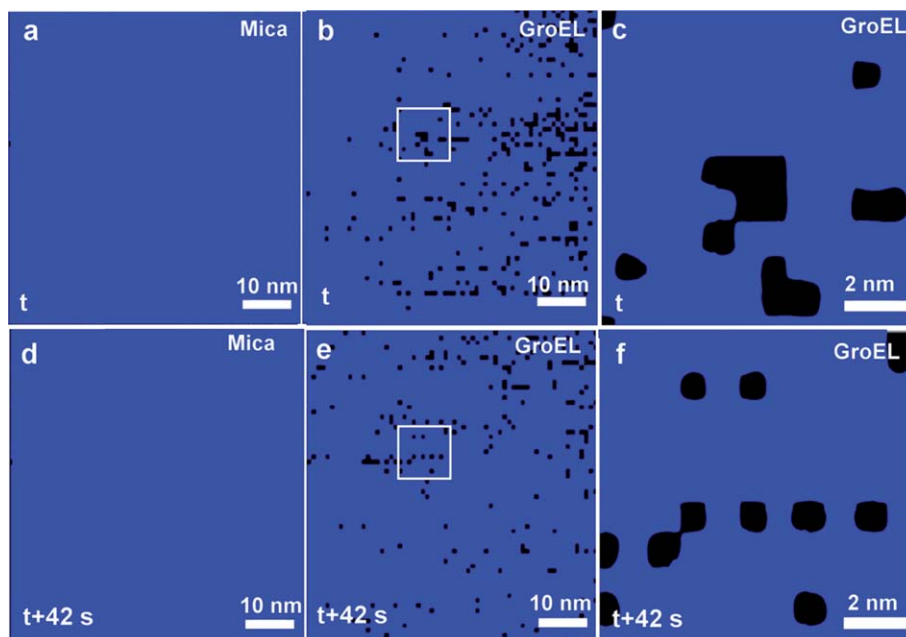


**Fig. 6** Map of the stability of mica and GroEL–water interfaces taken at 0.7 nm above the surface. The map records variations of the amplitude,  $\Delta A \geq 0.53 A_{01}$  ( $A_{01} = 500$  pm). No variations are seen on the mica–water interface while numerous dark spots are seen on the GroEL patch–liquid interface. The dark spots represent regions of instabilities. (a) Mica–water interface. (b) GroEL patch–water interface. (c) Zoom-in image of the region marked in (b). (d) Evolution of the mica–water interface shown in (a) after 42 s. (e) Evolution of the GroEL patch–water interface shown in (b) after 42 s. (f) Zoom-in image of the region marked in (e). The maps represent the instantaneous variation of the amplitude on an  $xy$  plane 0.7 nm above the mica and GroEL surfaces.

We remark that the above perturbations have only been observed in the GroEL–liquid interfaces. The comparison between the 3D hydration maps taken on mica and GroEL under similar conditions shows that the mica–water interface is free from those instabilities.

A quantitative comparison of the instabilities observed on mica and GroEL–water interfaces under similar conditions (scan size = 64 nm) is presented in Fig. 6. The figure shows a number of spots on the *xy* plane with strong variations in the amplitude ( $\sim 0.53 A_0$ ) at two different times. No such spots are seen on the mica–water interface while about 10% of the GroEL–liquid interface is covered by instability spots. The perturbations observed on the GroEL–water interface may be a consequence of the topographic variations over the GroEL molecules and patches or the compliance of the protein surface. The GroEL has a ring structure with a central opening and the protein arrays are not fully packed (Fig. 1b). There are some gaps between the proteins. Some modification or disruption in the hydration layer/nanoconfined water could be expected in those regions.

## 4 Conclusion

We have developed a force microscopy method to map the three-dimensional force fields and their time-evolution on solid–water interfaces. The method combines angstrom resolution, 10 pN force sensitivity and an image acquisition time in the sub-minute range. The method has mapped with atomic resolution mica and GroEL–water interfaces. In particular, hydration layers have been imaged with angstrom resolution. We have provided maps following the evolution of nanoscale water perturbations on GroEL–water interfaces. The observed perturbations involve force changes of several hundreds of pN. Those instabilities are not found in stiff and atomically flat interfaces. The ability to detect 3D force maps in those vastly different systems reflects the robustness of the method. We believe that three-dimensional maps with angstrom and piconewton resolutions could be applied to give a complete characterization of complex soft-matter–liquid interfaces such as the one encountered on cell surfaces.

## Acknowledgements

We are grateful for the financial support from the Ministerio de Economía y Competitividad (CSD2010-00024, MAT2009-08650); PRESTO, Japan Science and Technology Agency.

## References

- G. Binnig, C. F. Quate and C. Gerber, *Phys. Rev. Lett.*, 1986, **56**, 930.
- T. Uchihashi, R. Lino, T. Ando and H. Noji, *Science*, 2011, **333**, 755–758.
- Y. Gan, *Surf. Sci. Rep.*, 2009, **64**, 99–121.
- Y. Sugimoto, P. Pou, M. Abe, P. Jelinek, R. Perez, S. Morita and O. Custance, *Nat. Mater.*, 2007, **446**, 64–67.
- C. Barth, S. A. Foster, C. R. Henry and A. L. Shluger, *Adv. Mater.*, 2011, **23**, 477–501.
- C. Bustamante, Y. R. Chemla, N. R. Forde and D. Izhaky, *Annu. Rev. Biochem.*, 2004, **73**, 705–748.
- F. Rico, C. Su and S. Scheuring, *Nano Lett.*, 2011, **11**, 3983–3986.
- C. A. Bippes and D. J. Muller, *Rep. Prog. Phys.*, 2011, **74**, 086601.
- D. Boal, *The Mechanics of the Cell*, Cambridge University Press, Cambridge, 2nd edn, 2012.
- P. K. Hansma, G. Schitter, G. E. Fantner and C. Prater, *Science*, 2006, **314**, 601–602.
- J. Israelachvili, *Intermolecular and Surface Forces*, Elsevier Academic Press, London, 2005.
- H. J. Butt and M. Kappl, *Surface and Interfacial Forces*, Wiley-VCH, Weinheim, 2010.
- P. J. Feibelman, *Phys. Today*, 2010, **63**, 34–39.
- A. Verdaguer, G. M. Sacha, H. Bluhm and M. Salmeron, *Chem. Rev.*, 2006, **106**, 1478–1510.
- C. F. Simeone, C. Albonetti and C. Cavallini, *J. Phys. Chem. C*, 2009, **113**, 18987–18994.
- H. Holscher, S. M. Langkat, A. Schwarz and R. Wiesendanger, *Appl. Phys. Lett.*, 2002, **81**, 4428–4430.
- B. J. Albers, T. C. Schwendemann, M. Z. Baykara, N. Pilet, M. Liebmann, E. I. Altman and U. D. Schwarz, *Nat. Nanotechnol.*, 2009, **4**, 307–310.
- M. Z. Baykara, T. C. Schwendemann, E. I. Altman and U. D. Schwarz, *Adv. Mater.*, 2010, **22**, 2838–2853.
- T. Fukuma, Y. Ueda, S. Yoshioka and H. Asakawa, *Phys. Rev. Lett.*, 2010, **104**, 016101.
- K. Kimura, S. Ido, N. Oyabu, K. Kobayashi, Y. Hirata, T. Imai and H. Yamada, *J. Chem. Phys.*, 2010, **132**, 194705.
- R. Garcia and E. T. Herruzo, *Nat. Nanotechnol.*, 2012, **7**, 217–226.
- T. R. Rodriguez and R. Garcia, *Appl. Phys. Lett.*, 2004, **84**, 449.
- N. F. Martinez, S. Patil, J. R. Lozano and R. Garcia, *Appl. Phys. Lett.*, 2006, **89**, 153115.
- D. Martinez-Martin, E. T. Herruzo, C. Dietz, J. Gomez-Herrero and R. Garcia, *Phys. Rev. Lett.*, 2011, **106**, 198101.
- T. Fukuma, M. Kimura, K. Kobayashi, K. Matsushige and H. Yamada, *Rev. Sci. Instrum.*, 2005, **76**, 053704.
- T. Fukuma and S. P. Jarvis, *Rev. Sci. Instrum.*, 2006, **77**, 043701.
- T. Fukuma, *Rev. Sci. Instrum.*, 2009, **80**, 023707.
- J. Wang and D. C. Boisvert, *J. Mol. Biol.*, 2003, **327**, 843–855.
- S. J. O'Shea and M. E. Welland, *Langmuir*, 1998, **14**, 4186–4197.
- S. P. Jarvis, T. Uchihashi, T. Ishida, H. Tokumoto and Y. Nakayama, *J. Phys. Chem. B*, 2000, **104**, 6091–6094.
- T. D. Li, J. Gao, R. Szoszkiewicz, U. Landman and E. Riedo, *Phys. Rev. B: Condens. Matter*, 2007, **75**, 115415.
- S. Khan, G. Matei, S. Patil and P. Hoffmann, *Phys. Rev. Lett.*, 2010, **105**, 106101.
- S. De Beer, D. Van Ende and F. Mugele, *Nanotechnology*, 2010, **21**, 325703.
- K. Voitchovsky, J. J. Kuna, S. A. Contera, E. Tosatti and F. Stellacci, *Nat. Nanotechnol.*, 2010, **5**, 401–405.

- 35 A. Ulcinas, G. Valdre, V. Snitka, M. J. Miles, P. M. Claesson and M. Atognozzi, *Langmuir*, 2011, **27**, 103551.
- 36 A. Labuda, K. Kobayashi, D. Kiracofe, K. Suzuki, P. H. Grutter and H. Yamada, *AIP Adv.*, 2011, **1**, 022126.
- 37 D. Argyris, P. D. Ashby and A. Striolo, *ACS Nano*, 2011, **5**, 2215–2223.
- 38 J. E. Sader and S. P. Jarvis, *Appl. Phys. Lett.*, 2004, **84**, 1801–1803.
- 39 H. Shuiqing and A. Raman, *Nanotechnology*, 2008, **19**, 375704.
- 40 A. J. Katan, M. H. van Es and T. H. Oosterkamp, *Nanotechnology*, 2009, **20**, 165703.
- 41 J. E. Sader, T. Uchihashi, M. J. Higgins, A. Farrell, Y. Nakayama and S. P. Jarvis, *Nanotechnology*, 2005, **16**, S94–S101.
- 42 R. Garcia, C. J. Gomez, N. F. Martinez, S. Patil, C. Dietz and R. Magerle, *Phys. Rev. Lett.*, 2006, **97**, 016103.